


Article

A Comparative Study of Mn/Co Binary Metal Catalysts Supported on Two Commercial Diatomaceous Earths for Oxidation of Benzene

Marco Tomatis ^{1,2}, Honghui Xu ³, Chaohui Wei ², Matthew Thomas Bishop ², Jun He ^{1,2,*} , Chengjun Wang ⁴, Ming Zhao ^{5,*}, Hang Xiao ⁶ , Huan Yu ⁷, Sailesh N. Behera ⁸ and Bencan Tang ¹

- ¹ Research Group of Natural Resources and Environment, Department of Chemical and Environmental Engineering, University of Nottingham Ningbo China, Ningbo 315100, China; tomatis.marco@nottingham.edu.cn (M.T.); Bencan.tang@nottingham.edu.cn (B.T.)
- ² International Doctoral Innovation Centre, University of Nottingham Ningbo China, Ningbo 315100, China; zx17884@nottingham.edu.cn (C.W.); matt.bishop@nottingham.edu.cn (M.T.B.)
- ³ Zhejiang Meteorological Science Institute, Hangzhou 310051, China; xuhonghuiharry@gmail.com
- ⁴ College of Chemistry and Materials Engineering, Wenzhou University, Wenzhou 325035, China; cjwang@wzu.edu.cn
- ⁵ School of Environment, Tsinghua University, Beijing 100084, China
- ⁶ Center for Excellence in Regional Atmospheric Environment, Institute of Urban Environment, Chinese Academy of Sciences, Xiamen 361021, China; hxiao@iue.ac.cn
- ⁷ School of Environmental Science and Engineering, Nanjing University of Information Science and Technology, Nanjing 210044, China; hyu@nuist.edu.cn
- ⁸ Department of Civil Engineering, and Centre for Environmental Science and Engineering (CESE), Shiv Nadar University, Greater Noida, Uttar Pradesh 201314, India; sailesh.behera@snu.edu.in
- * Correspondence: jun.he@nottingham.edu.cn (J.H.); ming.zhao@mail.tsinghua.edu.cn (M.Z.); Tel.: +86-574-8818-0000 (ext. 9385) (J.H.); +86-010-6278-4701 (M.Z.)

Received: 27 January 2018; Accepted: 9 March 2018; Published: 12 March 2018

Abstract: Two commercial diatomaceous earths were used as supports for the preparation of Mn/Co binary metal catalysts at different metal loads (5 to 10 wt % Mn and 5 to 15 wt % Co) by incipient wetness deposition. The activity of the prepared catalysts towards the complete oxidation of benzene to CO₂ and water was investigated between 100 and 400 °C. Raw supports and synthesized catalysts were characterized by XRD, N₂ physisorption, SEM-EDS, H₂-TPR, and TPD. The purification treatment of food-grade diatomite significantly affected the crystallinity of this support while reducing its specific surface area (SSA). A loss of SSA, associated with the increase in the metal load, was observed on samples prepared on natural diatomite, while the opposite trend occurred with food-grade diatomite-supported catalysts. Metal nanoparticles of around 50 nm diameter were observed on the catalysts' surface by SEM analysis. EDS analysis confirmed the uniform deposition of the active phases on the support's surface. A larger H₂ consumption was found by TPR analysis of natural diatomite-based samples in comparison to those prepared at the same metal load on food-grade diatomite. During the catalytic oxidation experiment, over 90% conversion of benzene were achieved at a reaction temperature of 225 °C by all of the prepared samples. In addition, the formation of coke during the oxidation tests was demonstrated by TGA analysis and the soluble fraction of the produced coke was characterized by GC-MS.

Keywords: diatomaceous earth; benzene; volatile organic compounds; catalytic oxidation; incipient wetness deposition

1. Introduction

Volatile organic compounds (VOCs) are a class of chemicals emitted by natural and anthropogenic sources, such as vegetation, industrial processes, and transportation [1,2]. These pollutants are known as some of the main precursors for the formation of photochemical smog, resulting in the generation of harmful products [3]. VOCs also contribute to climate change as greenhouse gases and affect the ozone layer [3]. Due to their hazardous nature towards human health and the environment, the emission limits of VOCs from industrial sources and remediation activities are being lowered by regulatory agencies and organizations worldwide, including the Environmental Protection Agency (EPA, Washington, DC, USA) and the World Health Organization WHO [4,5]. The EPA especially focuses on the emissions of benzene, toluene, ethylbenzene, and xylene (BTEX), which are considered to be predominant pollutants because of their toxicity and elevated concentration levels from various emission sources.

Although the direct effects of these pollutants on human health cannot be precisely quantified, it is possible to indirectly evaluate them by exposure risk assessments. For example, an increase of around 465% in the incidence of lung cancer was observed in China over the last 30 years, which was found to be associated with long-term exposure to severe air pollution, also including exposure to VOCs [6].

The concentration levels of VOCs in waste gas streams before the treatment are often above the regulatory limits. Several processes, including thermal oxidation, biological treatments, and catalytic oxidation, were developed to lower the concentration of VOCs emitted in the contaminated gas to the levels required by regulations [7]. The catalytic oxidation of VOCs has been studied due to its efficiency in decomposing these pollutants into CO₂ and water at temperatures below 400 °C [8,9].

Various types of metals, metal composites, and supports have been examined for the degradation of VOCs [9]. Noble metals such as Pd, Pt, and Au were widely studied due to their activity and selectivity at low temperatures [8,10,11]. However, the disadvantages involved in the use of noble metals, such as high cost and low resistance to poisoning, directed the interest of the scientific community towards cheaper transition-metal-based catalysts [1,12–16]. Researchers have investigated a number of different transition metals and support materials, aiming to improve activity and selectivity of the prepared catalysts towards the complete oxidation of VOCs [1,13,17–19].

Diatomaceous earths are natural silicates composed of fossilized diatoms, aquatic unicellular algae from the tertiary and quaternary periods. Due to their origin, diatomaceous earths consist of amorphous silica with small quantities of microcrystalline material [20]. The presence of impurities can be observed on this material though their composition and content might vary based on the provenience of the diatomite [2,21]. Purified diatomaceous earths are used as a filtration media in various industrial areas, such as water treatment, pharmaceutical processing, and brewing [22–25]. According to the specifications of the raw material, the specific surface area (SSA) and other physical properties, including permeability, particle size, and pore size and distribution, can vary greatly depending on the pretreatment process. The purification treatment also tends to produce a more crystalline form of silica and more uniform particle size and pore size distribution. Diatomaceous earths offer low SSA (between 1 and 300 m²/g) compared to other materials widely employed as supports for the preparation of catalysts, such as activated carbon or MCM-41 [8,19,26,27]. Nonetheless, the physical properties of diatomite, including peculiar porous structure, high sorption ability, thermal stability, and permeability, made this material widely applicable in bioreactors and other applications, including chromatography and heterogeneous catalysis [24,28–30]. Due to its natural hydrophobicity, diatomite-supported catalysts are resilient to deactivation caused by the presence of water [31,32]. This property makes diatomite an ideal support for heterogeneous catalysis and other applications involving contact with an aqueous phase [31,32]. Different deposition methods were successfully tested on diatomaceous earths, demonstrating the feasibility of impregnation on diatomite [21,33,34]. However, until now the application of diatomaceous earths as support for the synthesis of catalysts for

the complete oxidation of VOCs has not been attempted, necessitating a systematic study to determine its performances for such an application.

Therefore, for the first time the capability of diatomaceous earth as a support for the preparation of catalysts to decompose of benzene into CO_2 and water was investigated. The influence of industrial purification treatment on the performance of food-grade diatomite as a support was also studied. The formation of heavy carbonaceous compounds inside the porous structure of the support has been widely reported for zeolites during the oxidation of VOCs [35–37]. Given the similarities of diatomaceous earths and zeolites, the potential formation of coke on diatomite-supported catalysts was also examined. Transition metals such as Mn and Co in either single or binary metal catalysts have been widely studied for their decomposition activity towards BTEX and, comparatively, the binary active phases generally outperformed the single one [1,9,12,13,38]. Hence, the binary metal catalysts containing Mn and Co were selected in this study, and were prepared by incipient wetness deposition. Preliminary tests on the activity of the single metal oxides were not included here. It is worth highlighting that the focus of this study was to demonstrate the suitability of diatomaceous earths as support for the catalytic decomposition of VOCs from the contaminated gas stream. Furthermore, the relative mass content of Mn and Co in the catalysts was to be optimized. The prepared catalysts, as well as the two raw materials, were characterized and tested to compare their catalytic activity for the oxidation of benzene in synthetic waste gas. The choice of benzene as a model compound for this study was not only dictated by the environmental hazards posed by this pollutant, but also by its toxicity, as benzene is classified as an A1 carcinogenic pollutant [39].

2. Results and Discussion

2.1. XRD Characterization

The crystal phase and crystallinity of the two raw supports and synthesized catalysts were studied by XRD analysis and presented in Figure 1a. The XRD pattern of food-grade diatomite showed well-defined diffraction peaks, compatible with the presence of crystalline silica (cristobalite JCPDS 39-1425), due to the purification treatment [40,41].

Based on the manufacturer's data sheet, during the purification process, the natural mineral, usually containing crystalline silica (cristobalite) less than 1 wt %, gets crushed and milled, dried in hot air, and winnowed through a cyclone in order to separate the different grain sizes and shapes. After this first step, diatomite is heated in a furnace at temperatures ranging between 980 and 1200 °C, roasted using sodium chloride, treated with sulfuric acid, and calcined.

The high-temperature treatment increases the crystallinity of silicate in food-grade diatomite due to the sintering of smaller crystals [42], producing the well-defined diffraction peaks shown in Figure 1a.

On the contrary, the natural diatomite produced a different diffraction pattern containing a single broad peak located at 21.9° (2θ), compatible with the presence of amorphous SiO_2 [34]. In agreement with the experimental results reported by Sun et al., no diffraction peaks associated with impurities were observed in the diffractogram of natural diatomite [34]. The absence of peaks for impurities was expected as their mass content (4.1 wt % Al_2O_3 , 1.6 wt % Fe_2O_3 , 0.4 wt % CaO and 0.2 wt % MgO) was below the limit of detection of the instrument. More pronounced background noise was also observed in the diffraction pattern of natural diatomite.

To investigate the crystal phase of deposited metal oxides, samples prepared at low and high metal loads on both supports (Mn_5Co_5 and $\text{Mn}_{10}\text{Co}_{15}$) were analyzed (Figure 1b). Characteristic diffraction peaks of Co_3O_4 crystallites (JCPDS 42-1467) were observed at 19.0° , 36.9° , 59.5° , and 65.3° (2θ). Less intense diffraction peaks were observed at 21.7° , 36.8° , and 64.8° (2θ) indicating the presence of $\gamma\text{-MnO}_2$ (ramsdellite, JCPDS 82-2169). The diffraction peaks of MnO_2 were hardly observed, while those of Co_3O_4 were clearly identifiable. Comparable peak intensities were observed for samples prepared at low and high metal loads on the same support (Mn_5Co_5 and $\text{Mn}_{10}\text{Co}_{15}$) [1].

The diffraction patterns of Mn_xCo_y/N and Mn_xCo_y/F appeared comparable, with the exception of the diffraction peaks of SiO_2 . Such peaks were distinctive on food-grade diatomite-supported samples due to the high content of crystalline SiO_2 . However, it was not possible to identify the diffraction peaks of single-phase Mn–Co mixed oxides on all prepared samples and such an absence of mixed metal oxides could be attributed to the preparation method used in this study, which is basically for the synthesis of binary metal catalysts but not mixed metal oxides. The observed small and broad diffraction peaks might be due to the effect of calcination temperature adopted in this study (250 °C) [26,43]. According to the experimental observations reported by Li et al., a low calcination temperature tends to reduce the sintering of the metal particles, which is potentially beneficial for producing a large number of active sites [43]. The number of active sites was associated with the active surface area of the catalyst and thus the catalytic activity [44,45]. The size of Co_3O_4 crystallites was calculated according to the Scherrer equation. Larger crystallites were observed on Mn_5Co_5/F and $Mn_{10}Co_{15}/F$ (63 and 78 nm, respectively) as compared to Mn_5Co_5/N and $Mn_{10}Co_{15}/N$ (23 and 35 nm respectively). On the contrary, it was not possible to apply Scherrer equation to MnO_2 as the peaks belonging to Mn oxides partially overlapped with other peaks (Figure 1). The formation of larger metal particles on food-grade diatomite was correlated with the SSA of this support (1.35 m^2/g) as it might offer less binding sites for the metal deposition as compared to natural diatomite (51.3 m^2/g). The size of cristobalite's crystallites on food-grade diatomite was around 30 nm.

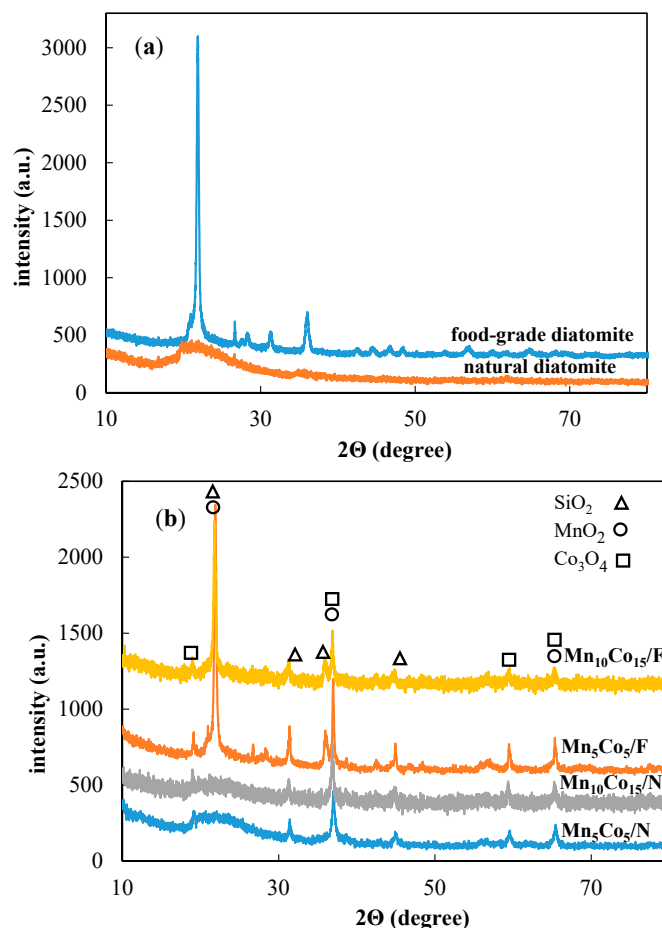


Figure 1. XRD patterns of (a) raw supports; (b) representative samples calcined at 250 °C.

2.2. Morphological and Textural Analysis

SEM images of both raw supports and representative catalysts are illustrated in Figure 2. As seen in Figure 2a, natural diatomite is composed of disk-like particles. This figure clearly shows the

exceptional diversity of sizes and morphologies typical of diatomaceous earths [34]. Such diversity appeared to be lost in the food-grade diatomite as the purification treatment allows for selecting particles of similar sizes, which generally possess beehive-like structures (Figure 2b). Nonetheless, similarities were also observed between these two raw support materials as they both exhibited a highly ordered porous structure (Figure 2a,b). Figure 2c,d presents the SEM micrographs at low magnification of Mn_xCo_y/N and Mn_xCo_y/F , respectively. As expected, the peculiar structure of the two diatomaceous earths could still be observed after the metal deposition.

To give an overview of the surface morphology and metal particle size for the synthesized catalysts, samples prepared at low, medium, and high metal loads were analyzed at higher magnifications. SEM images of the analyzed samples showed that both materials appeared to be ideal hosts for the deposition of metal nanoparticles, as shown in Figure 2e–j. In agreement with the experimental observations reported in Section 2.1, the presence of a large number of spherical particles of nanometrical scale was observed in all analyzed samples. For catalysts prepared using the same metal loads, both particle size and the distribution on the different supports appeared to be comparable. Different particle numbers per unit of surface area were observed on the tested catalysts. The particle density was associated with the metal load used to prepare the catalysts. In agreement with the findings reported by Zhou et al., aggregates were observed on those samples presented in Figure 2g–j [26]. Those aggregates were possibly caused by the undecomposed nitrates retained on the catalyst surface due to low calcination temperature. Nonetheless, as discussed in Section 2.1, low calcination temperatures were proven beneficial to the catalytic activity due to the reduced sintering of the active phase [26,43].

The absence of aggregates in Figure 2e,f did not exclude their existence on $Mn_{10}Co_{15}/N$ and $Mn_{10}Co_{15}/F$. On the contrary, it is plausible that aggregates were formed during the sample preparation due to their higher metal load. However, the purpose of the morphological characterization was to give an overview of the surface and metal particles. Hence, no efforts were made to locate them on every sample. The presence of both Mn and Co on all prepared catalysts was also confirmed by EDS analysis. Uniform dispersion of the active phases on the support's surface was observed on all analyzed samples during the EDS analysis. The SEM analysis did not reveal significant morphological differences between samples prepared on different supports.

SEM micrographs of spent catalysts, including $Mn_{10}Co_{15}/N$ and $Mn_{10}Co_{15}/F$, are reported in Figure 2k,l, respectively, and will be discussed in Section 2.5.

The specific surface area (SSA) and total pore volume of raw supports and representative catalysts are presented in Table 1. Large differences of SSA and pore volume were observed between the two raw supports. This difference was ascribed to the purification treatment, as after the milling different particle sizes were separated through winnowing in a cyclone. A narrow pore size distribution was observed in the food-grade diatomite. For this material, around 60% of the total pore volume ($0.001\text{ cm}^3/\text{g}$) was represented by pores of diameter ranging from 72 nm to 90 nm. A wider pore size distribution was observed on natural diatomite, with over 78% of the total pore volume ($0.173\text{ cm}^3/\text{g}$) distributed between pores of size ranging between 15 and 175 nm. Figure 3 reports the adsorption isotherms of the raw supports and samples prepared at the lowest and highest metal loads. As expected for the wide pore size distribution described for the natural diatomite, type IV isotherms showing a H4 hysteresis loop were observed on Mn_xCo_y/N and on the natural diatomite (Figure 3a). These results indicate that the internal structure of the natural diatomite was partially hollow, with internal voids of irregular shapes and broad size distribution. A significant decrease in the quantity of N_2 adsorbed by the samples with the increase of the deposited metal load was also observed (Figure 3a), which was associated with the formation of metal particles in the support's porous structure, causing the complete or partial occlusion of some of the pores [9]. A typical isotherm of pure silica (type II isotherm) was observed during the N_2 physisorption analysis of food-grade diatomite (Figure 3b) [46]. This result highlights the scarce porosity of food-grade diatomite as well as the macroporosity of this material (Table 1). On the contrary, type IV isotherms with H4 hysteresis loops were observed on Mn_xCo_y/F .

The different adsorption isotherm profiles observed during the tests could be attributed to the increase of the pore volume and the formation of a more complex porous structure. These experimental observations were ascribed to the deposited nanoparticles. Metal nanoparticles might exhibit a more complex morphology compared to the food-grade diatomite [47,48]. Therefore, the deposition of a large number of metal particles (Figure 2) had a significant influence on the surface properties of the diatomite.

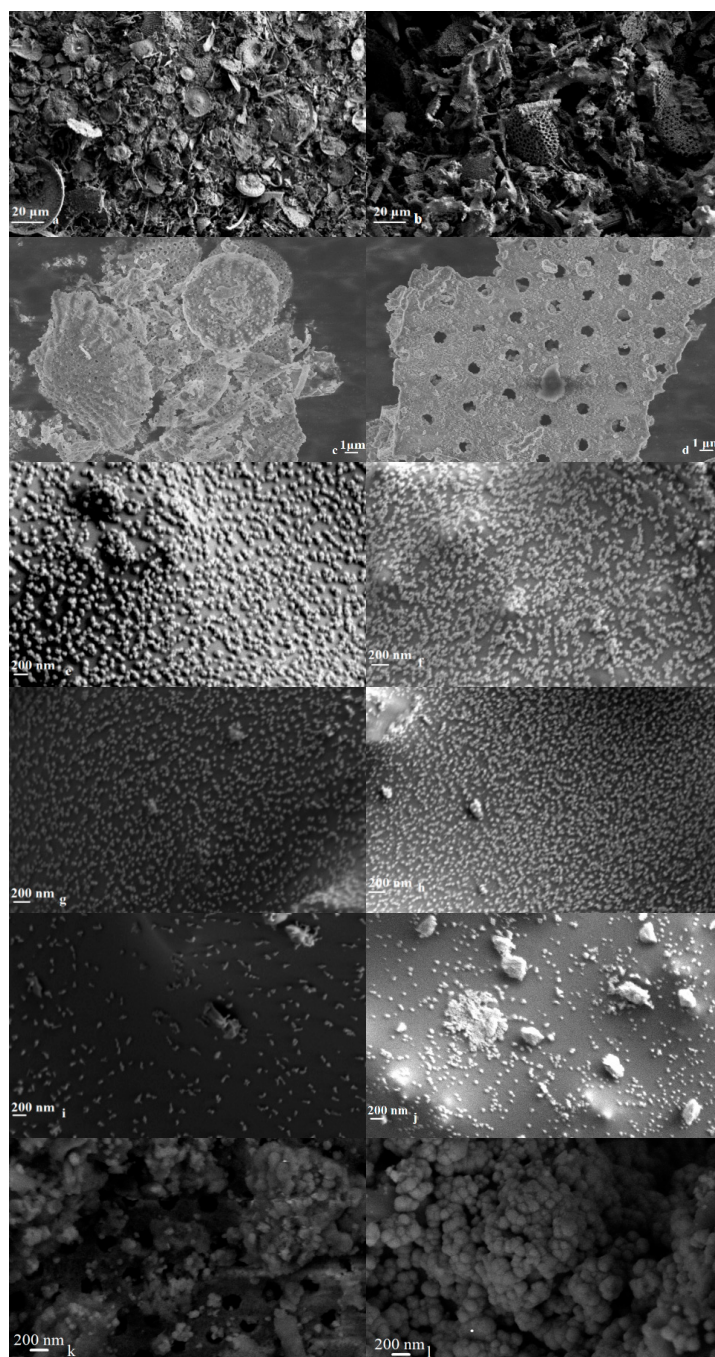


Figure 2. SEM images of (a) natural diatomite, (b) food-grade diatomite, catalysts calcined at 250 °C, including (c) Mn_xCo_y/N low magnification, (d) Mn_xCo_y/F low magnification, (e) $Mn_{10}Co_{15}/N$, (f) $Mn_{10}Co_{15}/F$, (g) $Mn_{10}Co_5/N$, (h) $Mn_{10}Co_5/F$, (i) Mn_5Co_5/N , and (j) Mn_5Co_5/F and used catalysts, including (k) $Mn_{10}Co_{15}/N$; (l) $Mn_{10}Co_{15}/F$.

Table 1. SSA and total pore volume of the raw supports and examined samples.

Sample	Mn wt %	Co wt %	BET SSA (m ² /g) ^a	Total Pore Volume (cm ³ /g) ^b
Natural diatomite	n.d.	n.d.	51.3	1.73×10^{-1}
Food-grade diatomite	n.d.	n.d.	1.35	6.84×10^{-4}
Mn ₁₀ Co ₁₅ /N	9.22	13.5	38.0	6.14×10^{-2}
Mn ₁₀ Co ₁₅ /F	8.98	13.8	14.1	2.09×10^{-2}
Mn ₁₀ Co ₅ /N	9.13	4.42	46.2	1.09×10^{-1}
Mn ₁₀ Co ₅ /F	9.18	4.74	10.8	1.99×10^{-2}
Mn ₅ Co ₁₅ /N	4.02	14.0	46.0	1.17×10^{-1}
Mn ₅ Co ₁₅ /F	4.15	13.9	8.84	1.44×10^{-2}
Mn ₅ Co ₅ /N	4.11	4.52	47.5	1.18×10^{-1}
Mn ₅ Co ₅ /F	3.82	4.26	5.45	7.70×10^{-3}

^a estimated by the BET method; ^b estimated by the BJH method on the desorption branch of absorption isotherm.

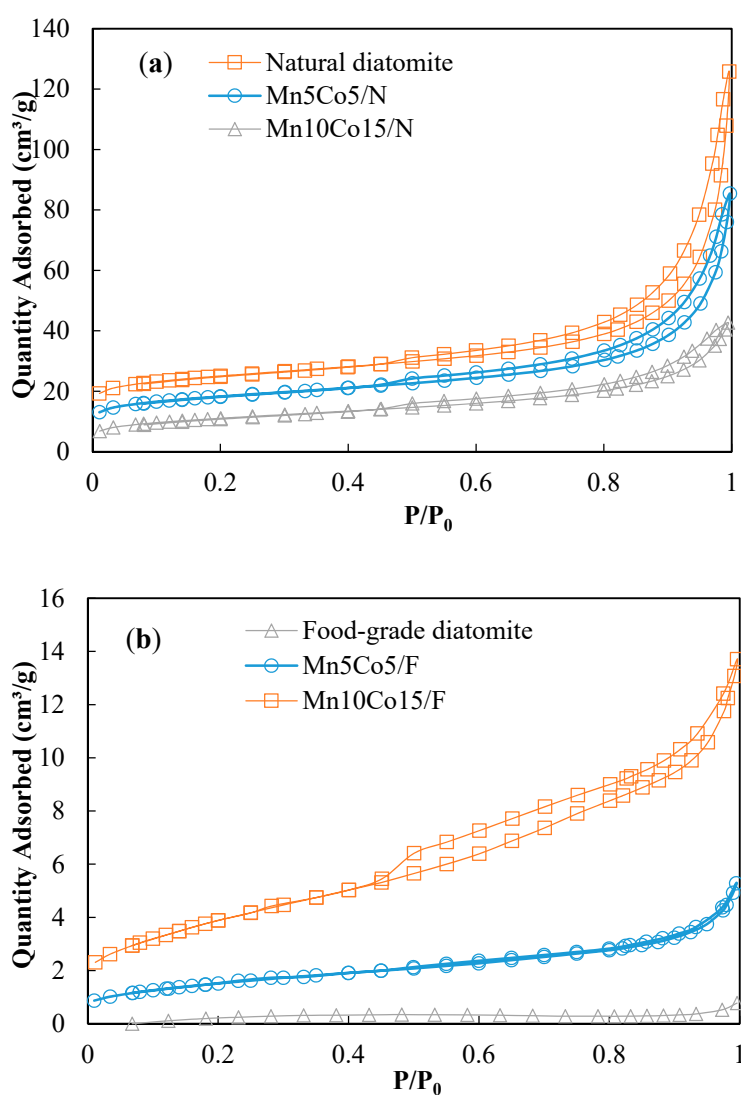


Figure 3. Adsorption isotherms of (a) natural diatomite and Mn_xCo_y/N; (b) food-grade diatomite and Mn_xCo_y/F.

2.3. TPR Studies

The reducibility of a catalyst determines, to a large extent, the activity towards VOCs oxidation [38,49]. Therefore, H₂-TPR analysis was conducted to investigate the reducibility of both raw supports and

representative catalysts. The TPR reduction profiles of two commercial diatomaceous earths are shown in Figure 4. It has been observed that both reduction profiles presented a well-defined peak at 366 °C. A small shoulder located around 430 °C was observed during the TPR analysis of natural diatomite. This maximum could be associated with the reduction of α -Fe₂O₃ to Fe₃O₄, which was in agreement with the composition of natural diatomite presented in Section 2.1 (1.6 wt % Fe₂O₃) [50]. It was not possible to observe additional reduction peaks related to further reduction of α -Fe₂O₃, probably due to the low metal content. Because of the presence of Fe₂O₃, the hydrogen consumption of natural diatomite (0.31 mmol H₂/g) was higher than what observed for food-grade diatomite (0.25 mmol H₂/g). Fe₂O₃ has been widely reported as an active phase for the catalytic oxidation of VOCs [51–53], and its presence on natural diatomite might provide a certain degree of activity towards the oxidation of VOCs when the reaction temperature is met.

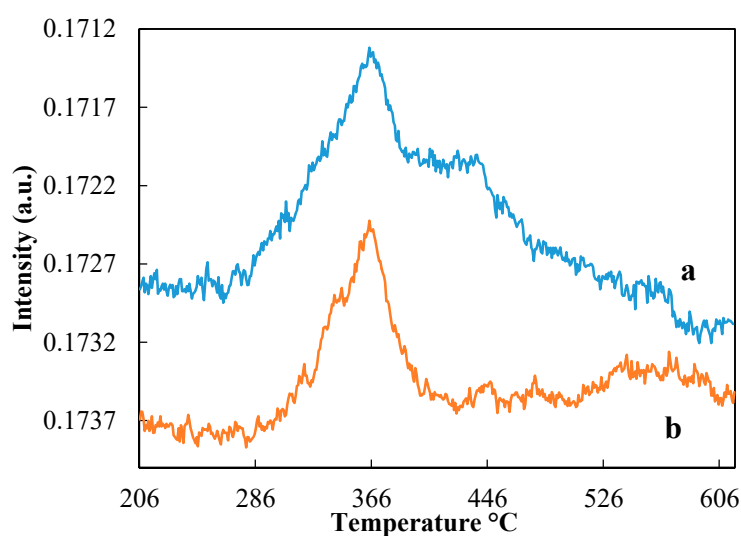


Figure 4. H₂-TPR profiles of (a) natural diatomite and (b) food-grade diatomite.

The reducibility and hydrogen consumption of prepared samples were also analyzed through H₂-TPR analysis and presented in Figure 5 and Table 2. In general, the reduction profiles were similar in all cases with two pronounced peaks, discerned at approximately 215 and 280 °C, respectively. In Figure 5a,b it was also possible to observe a third peak located at around 250 °C. In agreement with the experimental results reported in Section 2.1, the peak observed at 215 °C was correlated with the one step reduction of MnO₂ to MnO, while the peaks observed at 250 and 280 °C were associated with the reduction of Co₃O₄ to CoO and the subsequent reduction of CoO to metallic cobalt, respectively [54–56]. However, the peak located at around 250 °C was not visible in Figure 5c,d, and it is likely to overlap with more pronounced neighboring peaks. The total hydrogen consumption of selected Mn_xCo_y/N catalysts was higher than that of those counterparts on food-grade diatomite with the same metal loads (Table 2).

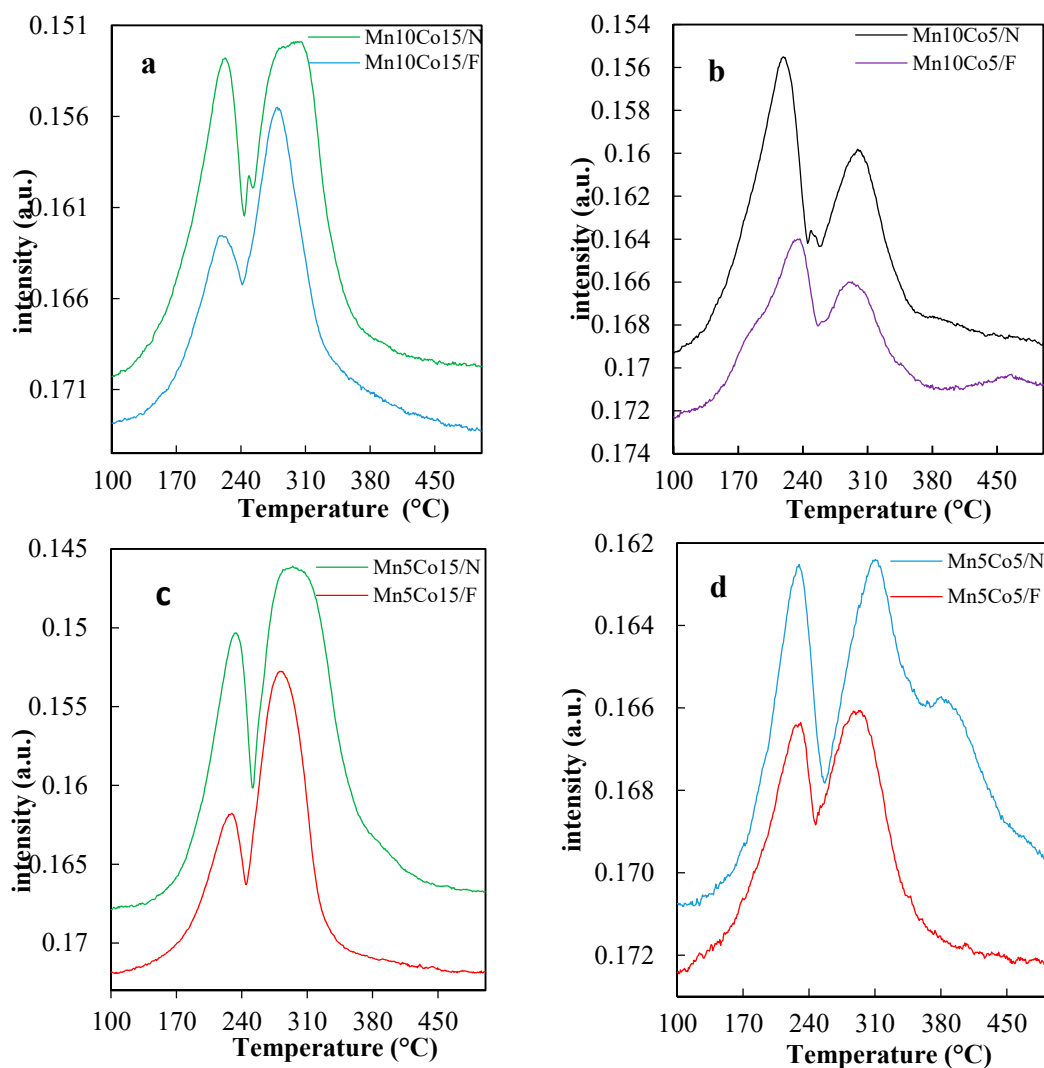


Figure 5. Comparison of the reduction profiles of (a) $Mn_{10}Co_{15}$, (b) $Mn_{10}Co_5$, (c) Mn_5Co_{15} , and (d) Mn_5Co_5 .

Table 2. Comparison of the total hydrogen consumption of the analyzed samples.

Sample	Natural Diatomite Total H_2 Consumption (mmol/g)	Food-Grade Diatomite Total H_2 Consumption (mmol/g)
$Mn_{10}Co_{15}$	5.56	3.85
$Mn_{10}Co_5$	3.29	2.71
Mn_5Co_{15}	5.00	3.20
Mn_5Co_5	2.73	1.40

2.4. Catalytic Activity Tests

The oxidation tests results presented in this section refer to the average values calculated after triplicate experiments were conducted on samples of the same type. Oxidation tests were carried out on both raw supports in order to confirm their activity towards the oxidation of benzene in the selected temperature range from 100 °C to 400 °C. No significant changes in the concentration of benzene were detected in the whole range of temperatures during oxidation tests of food-grade diatomite. On the contrary, the catalytic conversion of benzene by the natural diatomite did not occur until the reaction temperature reached 350 °C; benzene's concentration from 1000 ppmv to around 790 ppmv was

observed at 400 °C on the natural diatomite, indicating that some catalytic decomposition capability of this support could possibly be activated at a high reaction temperature. This difference might be due to the presence of 1.6 wt % Fe₂O₃, as discussed in Section 2.1. However, the maximum conversion of benzene for all examined samples was almost reached at 225 °C, as seen in Figure 6. Therefore, it is possible to infer that the presence of Fe₂O₃ does not make a significant contribution in the overall activity of Mn_xCo_y/N when the reaction temperature is below 350 °C.

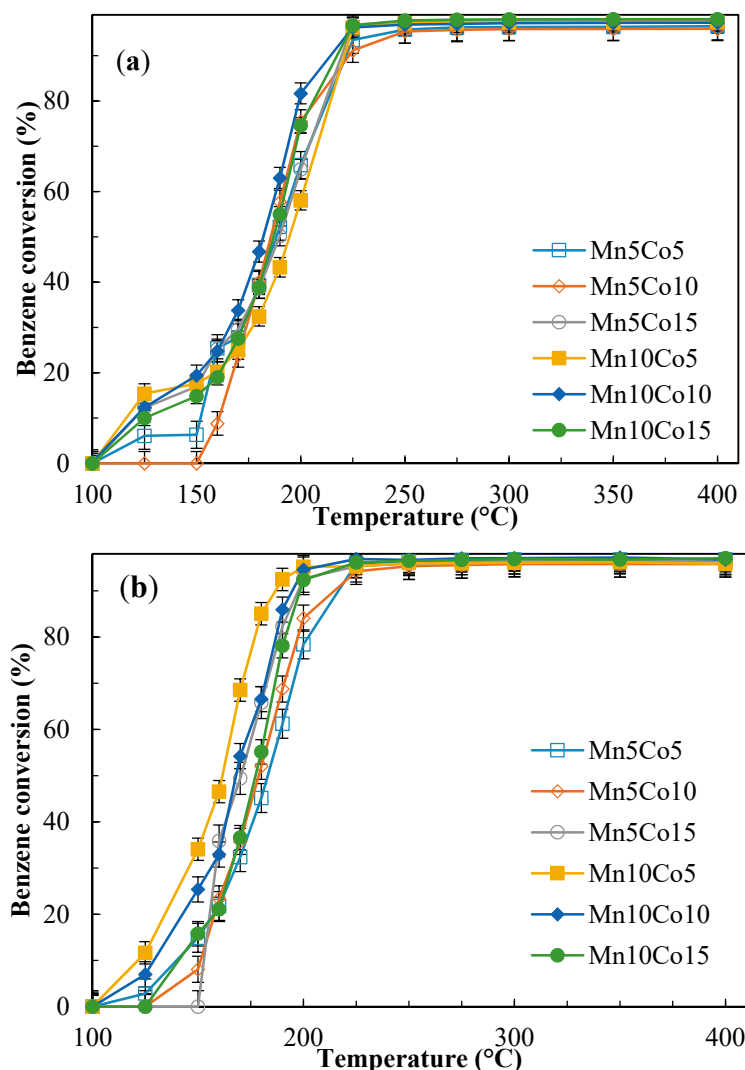


Figure 6. Average conversion rates of benzene estimated over three runs on (a) Mn_xCo_y/N and (b) Mn_xCo_y/F during the light-off experiments.

The conversion of benzene on Mn_xCo_y/N and Mn_xCo_y/F as a function of reaction temperature is shown in Figure 6. A monotonous decrease of benzene's concentration in the outlet gas has been observed until around 225 °C during the oxidation tests. Between 225 and 250 °C a plateau was reached, and further increasing the reaction temperature did not significantly lower the concentration of benzene in the outlet gas. It is noteworthy that all of the prepared samples surpassed 90% conversion at 225 °C. It is also worth highlighting that the maximum temperature reached during the oxidation tests (400 °C) was higher than the calcination temperature used for the synthesis of the catalysts (250 °C). Therefore, a certain degree of sintering of the active phase as well as the decomposition of nitrates might be expected at high reaction temperatures [26,43]. However, the activity of the analyzed catalysts appeared to have not been affected significantly by those changes in the structure of the

catalysts. Nonetheless, to investigate changes of the crystallinity and morphology of the used catalysts, SEM and XRD analysis of the spent $\text{Mn}_{10}\text{Co}_{15}/\text{N}$ and $\text{Mn}_{10}\text{Co}_{15}/\text{F}$ catalysts were performed and will be discussed in Section 2.5.

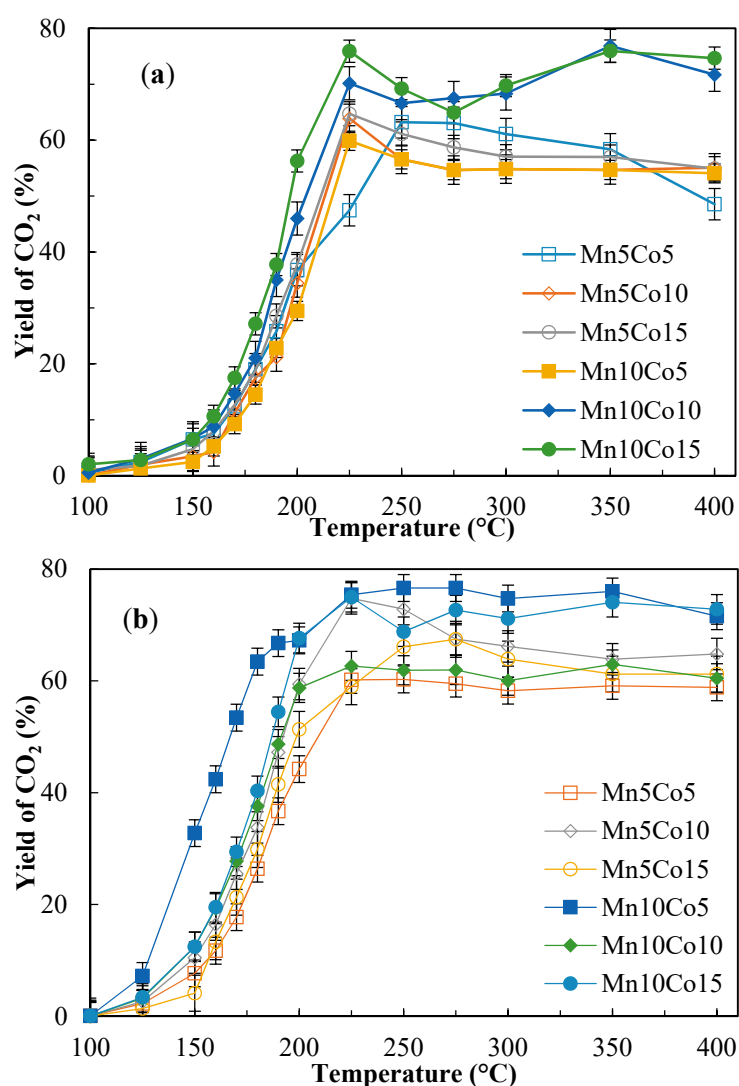
Although 225 °C can be considered the optimum temperature for catalytic oxidation of benzene in this study, only minor differences between the conversions of benzene by all tested catalysts on both natural and food-grade diatomites were observed at this temperature. Such differences were within range of the experimental errors calculated for the prepared samples (1.5 to 2.8%). Therefore, besides the conversions of benzene and yields of CO_2 at 225 °C, those recorded at 190 °C were also reported in Table 3 as this temperature was the lowest T90 observed in this study. The data reported in Table 3 clearly show that $\text{Mn}_x\text{Co}_y/\text{F}$ catalysts were more active at 190 °C in terms of both benzene decomposition and CO_2 yields before the light-off temperature 225 °C in comparison to their $\text{Mn}_x\text{Co}_y/\text{N}$ equivalents. However, from the results of the characterization tests, similar reduction temperatures were observed for the prepared samples (Figure 6); besides, based on the H_2 -TPD analysis (Table 4), a larger quantity of active phase appeared to be available on $\text{Mn}_x\text{Co}_y/\text{N}$ samples. It was also observed that, although no significant differences in the metal dispersion could be observed through XRD analysis, the size of the crystallites evaluated through the Scherrer equation seemed to be larger on $\text{Mn}_x\text{Co}_y/\text{F}$ samples. As mentioned above, it can be seen in Table 1 that the SSA of catalysts on food-grade diatomite was much lower than that of those on natural diatomite, while the total amounts of metals deposited were quite comparable. This indicates that the density of active phases (the mass per unit of SSA) on food-grade support was much higher, possibly leading to stronger catalytic conversion of benzene by food-grade-based catalysts before the performance of both types of catalysts stabilized to form the characteristic plateau on the light-off curve. The turnover frequencies (TOFs) of catalysts prepared at low (10 wt %), medium (15 wt %), and high (25 wt %) metal loads were evaluated to provide a more comprehensive comparison of the catalytic activities for conversion of benzene. The TOFs were evaluated based on reaction rates calculated below 10% conversion of benzene (Table 4) according to Equations (3) and (4) at the reaction temperature of 125 °C. Reaction rates on the order of 10^{-8} mol/s were observed for most analyzed samples, with the exception of $\text{Mn}_5\text{Co}_5/\text{N}$ and $\text{Mn}_5\text{Co}_5/\text{F}$. According to the results of the chemisorption analysis using hydrogen as a probe molecule, the quantity of active phase available on natural diatomite-based samples was almost 5–10 times that on $\text{Mn}_x\text{Co}_y/\text{F}$ (Table 4). Therefore, higher TOF values were estimated for $\text{Mn}_x\text{Co}_y/\text{F}$, as shown in Table 4. It is worth highlighting that higher TOFs values were estimated for $\text{Mn}_5\text{Co}_{10}/\text{N}$ and $\text{Mn}_5\text{Co}_{10}/\text{F}$ (26.2×10^{-5} and $210 \times 10^{-5} \text{ s}^{-1}$, respectively) compared to other samples on the same support. In addition, the TOFs of prepared catalysts were also investigated by considering the total metal load deposited on the catalysts. The latter approach indicates how much benzene can be converted per unit mass of active phase loading. As expected, the moles of active phase deposited on catalysts with the same mass ratio of Mn to Co prepared on different supports are comparable since $\text{Mn}_x\text{Co}_y/\text{N}$ and $\text{Mn}_x\text{Co}_y/\text{F}$ were prepared using almost the same metal load. Consequently, smaller differences of TOFs were observed between samples prepared on different supports, which were mostly related to the different reaction rates (see Equation (4)). Considering the total metal load, higher TOFs were obtained for $\text{Mn}_5\text{Co}_{10}/\text{N}$ and $\text{Mn}_5\text{Co}_{10}/\text{F}$ (7.56×10^{-5} and $5.63 \times 10^{-5} \text{ s}^{-1}$, respectively) compared to the rest of the catalysts on the same support. Based on both TOFs estimations, $\text{Mn}_5\text{Co}_{10}/\text{N}$ and $\text{Mn}_5\text{Co}_{10}/\text{F}$ (prepared on their respective supports) appear to be the most efficient catalysts for the degradation of benzene.

According to the results of the chemisorption analysis, it is plausible that $\text{Mn}_x\text{Co}_y/\text{F}$ would not be able to produce reaction rates comparable to those of $\text{Mn}_x\text{Co}_y/\text{N}$ in more challenging experimental conditions (i.e., higher GHSV and/or pollutant concentration) due to the lower quantity of metal phase available for the reaction [57]. This might need to be further investigated as the goal of this study was to determine if diatomaceous earths could be utilized as supports for the complete oxidation of VOCs in waste gas streams.

Table 3. Conversion rates of benzene and yields of CO₂ at reaction temperatures of 190 °C and 225 °C.

Sample	Benzene Conversion (%) at 190 °C		Benzene Conversion (%) at 225 °C		Yield to CO ₂ (%) at 190 °C		Yield to CO ₂ (%) at 225 °C	
	N ^a	F ^b	N ^a	F ^b	N ^a	F ^b	N ^a	F ^b
Mn ₁₀ Co ₁₅	55.0	78.1	96.7	96.1	37.8	54.5	75.9	74.9
Mn ₁₀ Co ₁₀	63.0	85.9	96.3	96.7	35.0	48.7	70.1	62.7
Mn ₁₀ Co ₅	43.3	92.5	96.3	95.3	22.8	66.8	60.0	75.4
Mn ₅ Co ₁₅	50.2	82.2	96.8	95.3	28.6	41.5	64.8	59.0
Mn ₅ Co ₁₀	57.7	68.8	91.1	94.2	21.1	47.2	63.9	74.7
Mn ₅ Co ₅	52.2	61.2	93.5	95.0	25.8	36.7	47.5	60.2

^a Natural diatomite as support; ^b Food-grade diatomite as support.

**Figure 7.** Average yields of CO₂ achieved over three runs on (a) Mn_xCo_y/N, (b) Mn_xCo_y/F during the light-off experiments.

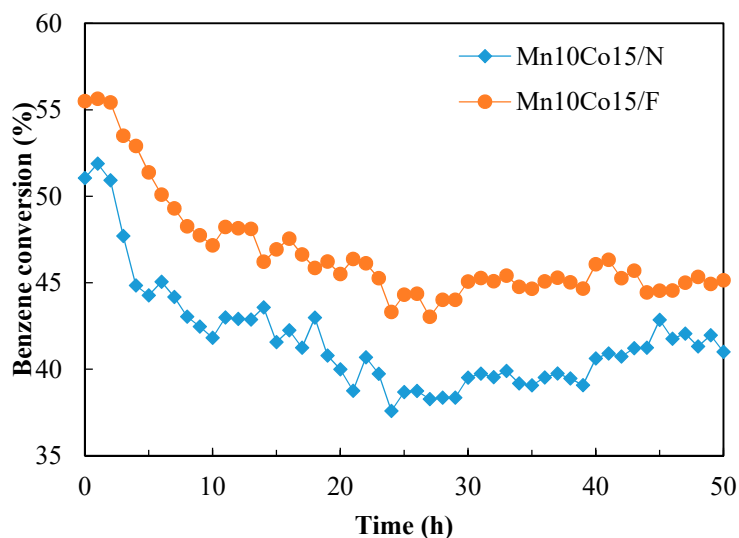


Figure 8. Stability tests results of $Mn_{10}Co_{15}/N$ and $Mn_{10}Co_{15}/F$ at 185 °C.

Table 4. Comparison of the turnover frequencies (TOFs) for the oxidation of benzene at 125 °C.

Sample	Reaction Rate (mol/s)	Moles of Available Active Phase (mol) $\times 10^{-5}$	TOF (s^{-1}) $\times 10^{-5}$ ^a	Total Moles of Active Phase (mol) $\times 10^{-4}$	TOF (s^{-1}) $\times 10^{-5}$ ^b
$Mn_{10}Co_{15}/N$	1.70×10^{-8}	17.2	9.90	11.9	1.43
Mn_5Co_{10}/N	5.12×10^{-8}	19.6	26.2	6.77	7.56
Mn_5Co_5/N	6.87×10^{-10}	11.6	0.592	4.55	0.151
$Mn_{10}Co_{15}/F$	4.03×10^{-8}	2.40	168	11.9	3.38
Mn_5Co_{10}/F	3.91×10^{-8}	1.85	210	6.94	5.63
Mn_5Co_5/F	0.999×10^{-8}	2.63	38.0	4.25	2.35

^a Evaluation based on the quantity of available active phase; ^b Estimated according to the total metal load.

During all catalytic activity tests, only chromatographic peaks belonging to CO_2 and H_2O were detected, indicating the absence of volatile and potentially hazardous by-products. As seen in Table 3, significant differences between the samples prepared on different supports were observed for the yields of CO_2 . In addition, differences in CO_2 yields were also evident between samples prepared on the same support, as shown in Figure 7. The discrepancy between benzene conversion and CO_2 yield and the absence of volatile byproducts of a reaction could be attributed to the formation of coke on the support's surface, as is commonly observed during the oxidation of benzene by other catalysts [58–60]. The formation of coke was studied and the results will be presented in Section 2.5.

Stability tests were conducted on $Mn_{10}Co_{15}/N$ and $Mn_{10}Co_{15}/F$ to determine their stability upon the formation of coke on the catalyst's surface. These two samples were selected as they showed the highest benzene conversion at 225 °C. For these tests, the temperature was kept constant at 185 °C for 50 h. This temperature was chosen as it was the T50 of $Mn_{10}Co_{15}/N$. Results from the stability tests are reported in Figure 8. The benzene conversion was stable for the first 2 h on both samples. Between 2 and 4 h, a decrease in conversion of around 5% was observed for $Mn_{10}Co_{15}/N$. The conversion of benzene slowly decreased until 24 h of reaction to around 40%. After reaching this minimum, the conversion became stable for the duration of the experiment. The conversion of benzene on $Mn_{10}Co_{15}/F$ monotonously decreased for 27 h of reaction from its initial 56% conversion to 43%. As observed for $Mn_{10}Co_{15}/N$, after reaching the minimum conversion, no further decreases in the activity of $Mn_{10}Co_{15}/F$ were observed during the entire test.

2.5. Characterization of the Used Catalyst

Significant differences between the conversion of benzene and yield of CO_2 were observed, as reported in Table 3. In addition, no volatile products other than CO_2 and H_2O were detected during the catalytic activity tests, as discussed in Section 3.4. These observations suggested that part of the

benzene somehow remained trapped in the porous structure of diatomite and retained under the form of heavy products of reaction (coke). Hence, the coke analysis was conducted for the used catalysts prepared on both supports by TGA and GC-MS.

The axial distribution of coke in the catalyst bed was not investigated in this study, as the sole purpose of this qualitative analysis was to demonstrate the formation of coke during oxidation tests to help in understanding the carbon balance. Therefore, the whole catalyst bed was analyzed and the results presented in Table 5 are not representative of the spatial distribution of the coke.

Based on the results shown in Table 5, a larger amount of coke of around 7 ~10 wt % was detected on Mn_xCo_y/N , while around 1 ~1.5 wt % was detected on Mn_xCo_y/F . In addition, only minor variations of coke content were observed among samples prepared on the same support, indicating that the duration of oxidation tests appeared to be sufficient to stabilize the coking formation. The formation of coke is usually observed inside the porous structure of catalyst, eventually in areas not covered by the active phase, and its growth in time leads to the deactivation of catalyst [43,58]. Li et al. also reported that the support's porous structure might influence the quantity of coke deposited [61]. For Mn_xCo_y/F , most of the pore volume, between 88% and 95% for Mn_5Co_5/F and $Mn_{10}Co_{15}/F$, respectively (Table 1), was formed during the metal deposition. It is possible to hypothesize that most of the porous structure of these samples is formed by the active phase and, as such, it would be more resistant to the formation of coke compared to the pure SiO_2 surface.

According to the results of the GC-MS analysis and the qualitative identification using the NIST mass spectrometry database, the soluble fraction of coke was composed of aromatic hydrocarbons and aromatic oxygenated compounds, as shown in Figure 9. In agreement with the observations reported by Pinard et al. and Rojo-Gama et al., lower weight hydrocarbons such as alkylbenzenes were detected at retention times ranging from 7 to 17 min, while at higher retention time, heavier polycyclic hydrocarbons including alkyl-naphthalene, alkylanthracenes, and phenanthrenes were found (Table 6) [58,59]. Due to the fact that the selected active phases, reaction temperature, and reaction time were kept the same for all catalytic oxidation tests [58,62], no significant change of coke composition was observed among the samples analyzed.

The crystallinity and morphology of used $Mn_{10}Co_{15}/N$ and $Mn_{10}Co_{15}/F$ were also investigated to determine if the application of high temperatures during the oxidation tests affected the structure of the spent catalysts [42]. Better resolved diffraction peaks were clearly observed during the XRD analysis of the spent samples (Figure 10) compared to those reported in Figure 1. These results indicated that the crystallinity of the deposited metals might have increased due to the exposure to reaction temperatures adopted during the oxidation tests higher than the calcination temperature (250 °C), which caused sintering of the active phase [42]. The crystal size of the deposited metal nanoparticles was also evaluated using the Sherrer equation. The size of Co_3O_4 crystallite increased from around 78 nm (on fresh sample) to 214 nm. Smaller crystallites were observed on the spent $Mn_{10}Co_{15}/N$ and their size was increased from 35 nm (on fresh sample) to around 103 nm. Due to the intensity of the diffraction peaks, it was also possible to estimate the crystal size for MnO_2 , which was 24 and 42 nm for $Mn_{10}Co_{15}/N$ and $Mn_{10}Co_{15}/F$, respectively.

In agreement with the results observed from XRD analysis, some differences were also observed in the SEM micrographs of the spent catalysts as compared to the corresponding fresh samples (Figure 2). The existence of metal particles of size around 100 nm was observed on used $Mn_{10}Co_{15}/N$ as shown in Figure 2k. Those large particles appear to have formed by the aggregation of smaller particles, as expected from the sintering of the active phase [42]. Aggregates of similar morphology but larger size were also observed on $Mn_{10}Co_{15}/F$, as shown in Figure 2l. The formation of larger aggregates observed on $Mn_{10}Co_{15}/F$ might be related to the lower specific surface area of this support as the higher density of metal particles on the support surface might promote the formation of larger aggregates [9,63].

Table 5. TGA analysis result for the used samples.

Sample	Coke Content (wt %)	
	Natural Diatomite	Food-Grade Diatomite
Mn ₁₀ Co ₁₅ (50 h)	8.96	1.45
Mn ₁₀ Co ₁₅	8.25	1.18
Mn ₁₀ Co ₁₀	7.21	1.26
Mn ₁₀ Co ₅	10.2	1.07
Mn ₅ Co ₁₅	8.22	1.14
Mn ₅ Co ₁₀	8.26	1.18
Mn ₅ Co ₅	7.40	1.22

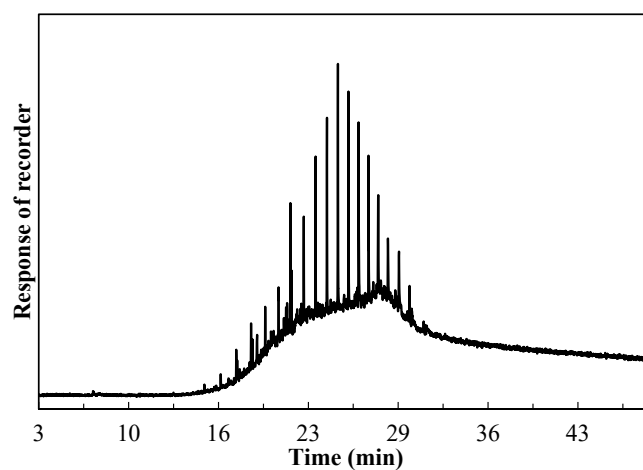
Figure 9. Chromatograms of the carbonaceous compounds retained on Mn₅Co₁₅/F.

Table 6. Molecular composition of the soluble fraction of the coke.

Family	Formula	<i>m/z</i> Range
Alkylbenzene	C _n H _{2n-6} (<i>n</i> > 6)	120–238
Alkyl-naphthalene	C _n H _{2n-12} (<i>n</i> > 10)	194–220
Alkylphenanthrene	C _n H _{2n-18} (<i>n</i> > 14)	206–250
Alkylanthracene	C _n H _{2n-18} (<i>n</i> > 14)	206–250

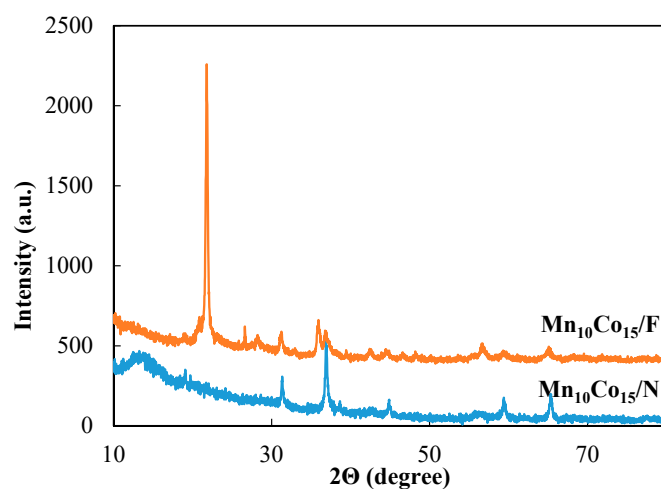


Figure 10. Diffractogram of the spent catalysts.

3. Experimental

3.1. Catalyst Preparation

Two commercial diatomaceous earths were selected as supports: Celite[®] S (Sigma-Aldrich, St. Louis, MO, USA) and food-grade Celite[®] (Celite Corporation, Lompoc, CA, USA). The composition of Celite[®] S was typical as non-pretreated diatomites including SiO₂ 93.7 wt %, Al₂O₃ 4.1 wt %, Fe₂O₃ 1.6 wt %, CaO 0.4 wt % and MgO 0.2 wt % [34,64]. This material was referred to as “natural diatomite” since it is not pre-treated after its extraction. On the contrary, the purified diatomite did not contain any impurities. Prior to sample preparation, both materials were washed with abundant ultrapure water to remove potential impurities deposited on their surface. The washed materials were then dried in a ventilated oven at 100 °C overnight to ensure complete evaporation of water from their porous structure.

Binary metal catalysts containing 5 or 10 wt % of Mn and 5, 10 or 15 wt % of Co were prepared by incipient wetness (IW) deposition. Firstly, aqueous solutions of Mn(NO₃)₂ (Sinopharm) were prepared dissolving 0.685 or 1.371 g, representing 5 and 10 wt % metal loads of the precursor salts in 3.500 mL of water, 50 µL of which were then added at a time to 2.850 or 2.700 g of diatomaceous earth under vigorous stirring, respectively. The samples were sonicated for 30 min and dried at 120 °C overnight in a ventilated oven, then washed and dried again. The dried samples were calcined at 250 °C for 3 h. For impregnation of the second metal, 0.741, 1.482, or 2.222 g of Co(NO₃)₃ (Sinopharm) as the precursor salt got dissolved in 3.000 mL of ultrapure water and these solutions were then added to the prior Mn-containing samples gradually, achieving 5–15 wt % Co-containing samples. The drying and calcination processes were conducted as described in the first-round impregnation of Mn. The catalysts were named Mn_xCo_y/N or Mn_xCo_y/F, where x and y represent the wt % of Mn and Co used for the impregnation, and N and F represent the natural and food-grade diatomite used as supports, respectively.

3.2. Characterization of Catalysts

The morphological studies were carried out on a Zeiss SIGMA Scanning Electron Microscopy (SEM) equipped with a Schottky field emitter operating at 2.0 kV and a beam current of 1.0 mA, and the data were collected on an ET-SE (Everhart–Thornley) type detector. Elemental analysis was performed by Energy Dispersive Spectroscopy (EDS) on an X-Act (Oxford Instrument, Abingdon-on-Thames, UK), coupled with the abovementioned SEM.

The X-ray diffraction (XRD) patterns were obtained by means of a D8 Advance diffractometer (Bruker) equipped with a copper anode (Cu-K α radiation $\lambda = 0.154$ nm). The scattering intensities were measured over an angular range of $10^\circ < 2\theta < 90^\circ$ with a step size of 0.01° on the high angle range and a count time of 2 s per step for all the samples.

The SSA and pore volume of samples were determined on the basis of low-temperature N₂ adsorption–desorption at -196 °C using ASAP 2020 (Micrometrics, Norcross, GA, USA) BET surface area analyzer after the initial degassing, at 350 °C for 6 h. The average pore size was calculated using the Barrett–Joyner–Haelanda (BJH) method using the desorption branch of the adsorption isotherm. The SSAs were calculated using the Brunauer–Emmet–Teller (BET) method. Samples of 0.1–1 g were used for the N₂ physisorption analysis in order to provide a minimum of 1 m² surface area to be measured, as suggested by the IUPAC guidelines [65].

Temperature-programmed reduction (TPR) analyses were performed on an AutoChem II 2920 (Micrometrics, Norcross, GA, USA) equipped with a TCD detector. To calibrate the analytical instrument, different sets of self-prepared gas mixtures of known compositions were prepared, applied, and analyzed for developing a calibration curve. Preoxidation of the samples and removal of the absorbed species from the catalyst surface was conducted following a procedure similar to that described by Saquer et al. [66]. The sample (30 mg) was placed in the u-shaped quartz microreactor and preoxidized for 30 min at 300 °C using a mixture of 3% O₂/He. The sample was then heated at

500 °C, under helium flow for 30 min to ensure the removal of adsorbed species from the catalyst surface, and cooled down to room temperature. The TPR tests were conducted on the preoxidized samples using hydrogen as a reducing agent (H₂-TPR). Under a flow of 10% H₂/He with flow rate 40 cm³/min, the samples were heated from 25 to 800 °C at a constant rate of 5 °C/min.

H₂ temperature-programmed desorption (H₂-TPD) analyses were performed using the same apparatus as for the TPR analysis. The sample (0.1 g) was firstly reduced in situ in a flow of 10% H₂/He at 300 °C for 2 h. After that, the sample was cooled down to 50 °C and saturated in 10% H₂/He for 1 h, followed by purging with N₂ for 30 min to remove any physisorbed molecules. H₂-TPD experiment was then operated at 800 °C with a heating rate of 5 °C/min under continuous flow of N₂.

3.3. Determination of the Catalytic Activity

The catalytic activity tests were carried out in a conventional quartz tubular reactor (6 mm i.d.) at atmospheric pressure and in the temperature range of 100–400 °C. Liquid benzene (Sinopharm, Beijing, China) was used to produce the feed gas without further treatment. An air stream, flowing through a saturator bottle containing an appropriate amount of liquid benzene, carried the VOC vapors to a mixing chamber, where a second air stream was used to dilute its concentration to the desired value (1000 ppmv). The space velocity (GHSV) was maintained constant in all experiments at 24,000 mL g⁻¹ h⁻¹ (calculated at STP) [9,18,27].

All runs were performed using 0.3 g of catalyst in powder form, and placed in the middle of the reactor, supported by quartz wool.

The concentration of benzene in the outlet gas was determined online by gas chromatography (GC Agilent Technologies 7890A, Santa Clara, CA, USA) using a flame ionization detector (FID). A HP-5 capillary column (15 m, 0.320 mm i.d., 0.25 μm stationary phase thickness) was selected for the separation of the organics. The benzene conversion rate was estimated using the following equation (Equation (1)):

$$\text{Conversion} = 1 - \frac{[\text{benzene}]_{\text{out}}}{[\text{benzene}]_{\text{in}}}, \quad (1)$$

where [benzene]_{out} and [benzene]_{in} represent the outlet and inlet concentration of benzene, respectively.

The concentration of CO₂ was determined by a thermal conductivity detector (TCD) using a HP-PLOT/Q capillary column (15 m, 0.320 mm i.d., 0.20 μm stationary phase thickness). The yield of CO₂ was estimated as follows:

$$\text{Yield} = \frac{[\text{CO}_2]_{\text{out}}}{([\text{benzene}]_{\text{in}} - [\text{benzene}]_{\text{out}}) \times n_c}, \quad (2)$$

where [CO₂]_{out} represents the outlet concentration of CO₂ and n_c represents the number of carbon atoms of benzene.

The turnover frequencies (TOF) of substrate conversion were calculated as follows:

$$\text{TOF} \left(\text{s}^{-1} \right) = \frac{\text{Rate of reaction}}{\text{H}_{2\text{ads}} \times \text{stoichiometry factor}} \times V_{\text{mH}_2} \times \text{catalyst weight} \quad (3)$$

$$\text{TOF} \left(\text{s}^{-1} \right) = \frac{\text{Rate of reaction}}{\text{moles of active phase in 0.3 g of catalyst}} \quad (4)$$

where the rates of reaction were evaluated according to a first-order kinetic between 0% and 10% conversion at the reaction temperature of 125 °C. The moles of accessible active phase were calculated based on the results of the H₂ chemisorption tests, according to the following factors, including the quantity of H₂ adsorbed (cm³/g), the stoichiometry factor of the reaction between H₂ and the selected metal, the molar volume of H₂ at STP (22.73 L/mol) and the weight of catalyst (0.3 g). To estimate the moles of active phase in 0.3 g of catalysts the total metal load deposited on the catalysts was considered instead of the moles of active phase available for the reaction.

3.4. Coke Analysis

The amount of total coke (C, wt %) retained on the catalyst after the oxidation test was determined through thermogravimetric analysis (TGA) using a Seiko SII Exstar 6000 thermal analyzer. During the analysis, the sample was heated at 10 °C/min between 25 and 1000 °C in a synthetic air stream, following a procedure developed for zeolites [35,36].

The soluble fraction of the coke was determined following the Guisnet method [37]. Briefly, the samples were dissolved using a solution of hydrofluoric acid 40%, and the soluble fraction of coke recovered in dichloromethane (CH₂Cl₂). The extracted components were characterized by GC-MS analysis using an Agilent7890 GC with a HP5-MS capillary column (30 m, 0.25 mm i.d., 0.25 μm stationary phase thickness) coupled with an Agilent5975 mass spectrometer. The identification of main components in the soluble fraction of the coke was acquired from the library search (NIST).

4. Conclusions

The two industrial diatomaceous earths were fully characterized and explored as support materials for the preparation of catalysts at different metal loads for the catalytic decomposition of benzene to CO₂ and water.

XRD characterization showed clear differences between the two raw supports as the purification process influenced the crystallinity of food-grade diatomite. The XRD analysis allowed identifying γ-MnO₂ and Co₃O₄ as the crystalline form of the two active phases. However, only small and broad diffraction peaks belonging to the metal oxides were observed during the analysis. Thus, only the size of Co₃O₄ crystallites could be calculated through the Scherrer equation. Smaller crystallites were observed on Mn_xCo_y/N in comparison to that Mn_xCo_y/F. The size of the crystallites increased with the metal load (23 and 35 nm for Mn₅Co₅ and Mn₁₀Co₁₅, respectively). SEM images of the raw supports showed similarly ordered porous structures on both diatomaceous earths. For the prepared catalysts spherical metal particles of size around 50 nm were observed. EDS results confirmed the presence of both Mn and Co on all tested catalysts as well as their uniform dispersion on the surface of the support. Large differences in SSAs were detected during N₂ physisorption analysis, indicating that the purification process affected the SSA, total pore volume and pore size distribution of food-grade diatomite. Based on the total hydrogen consumption, TPR analysis showed the higher reducibility of Mn_xCo_y/N compared to their equivalents on food-grade diatomite, which could be attributed to the more quantity of available active phase on this support. According to the TPD results, the moles of active phase available on Mn_xCo_y/N were around 10 times those estimated for Mn_xCo_y/F. The catalytic activities of the raw supports and catalysts were also evaluated and it was observed that the prepared catalysts reached their maximum conversion at temperatures in the range between 225 and 250 °C. The similar conversion rates observed during the oxidation tests were associated with the experimental conditions used for this study. However, the scope of this study was to determine if diatomaceous earths could offer a novel, cheap, and widely available support for the preparation of catalysts to be used for the complete oxidation of VOCs. As such, a relatively low GHSV was selected for this study. The presence of coke and its soluble fraction were confirmed and characterized by TGA and GC-MS analysis, respectively. The morphological and XRD analysis of spent catalysts clearly showed the aggregation of metal nanoparticles due to the exposure to high reaction temperatures. Metal aggregates of dimension around 214 nm were observed on Mn₁₀Co₁₅/F, while smaller metal particles (around 103 nm diameter) were detected on Mn₁₀Co₁₅/N. The lower surface area of food-grade diatomite influenced the density of the deposited metal nanoparticles and therefore might have promoted the formation of larger aggregates observed on Mn₁₀Co₁₅/F.

In summary, both natural and food-grade diatomite-supported catalysts containing Mn and Co showed very comparable catalytic activities for the oxidation of benzene into CO₂ and H₂O when stabilized to form the characteristic plateau on the light-off curve. Nonetheless, the physical characteristics observed for natural diatomite-based catalysts suggest that Mn_xCo_y/N might be better

catalysts as compared to $\text{Mn}_x\text{Co}_y/\text{F}$ when the treatment conditions become harsher in terms of larger GHSV and a higher concentration of target pollutants.

Acknowledgments: The authors acknowledge financial support from the International Doctoral Innovation Centre, Ningbo Education Bureau, Ningbo Science and Technology Bureau, and the University of Nottingham. This work was also partially supported by a Ningbo Innovation Team Project (2017C510001), the State's Key Project of Research and Development Plan of China (2016YFC0201901), the Zhejiang Provincial Applied Research Program for Commonweal Technology (2015C33011), the UK Engineering and Physical Sciences Research Council (EP/G037345/1 and EP/L016362/1), and the National Natural Science Foundation of China (41303091 & 91544229). The authors are also grateful in particular to Sheila Lee Dignazio for proofreading the manuscript and providing language polishing help.

Author Contributions: Marco Tomatis conceived, designed, and performed the synthesis of catalysts, SEM-EDS analysis, BET analysis, XRD analysis, catalytic activity tests, and GC-MS analysis. Chaohui Wei performed the TGA tests. The manuscript was written by Marco Tomatis. All other coauthors contributed to the analysis and interpretation of data, proofreading, and quality improvement of this report.

Conflicts of Interest: The authors declare no conflict of interest.

References

1. Zeng, J.; Liu, X.; Wang, J.; Lv, H.; Zhu, T. Catalytic oxidation of benzene over $\text{MnO}_x/\text{TiO}_2$ catalysts and the mechanism study. *J. Mol. Catal. A Chem.* **2015**, *408*, 221–227. [CrossRef]
2. Yu, W.; Deng, L.; Yuan, P.; Liu, D.; Yuan, W.; Liu, P.; He, H.; Li, Z.; Chen, F. Surface silylation of natural mesoporous/macroporous diatomite for adsorption of benzene. *J. Colloid Interface Sci.* **2015**, *448*, 545–552. [CrossRef] [PubMed]
3. Finlayson-Pitts, B.J.; Pitts, J.N., Jr. *Chemistry of the Upper and Lower Atmosphere*; Elsevier Inc.: Amsterdam, The Netherlands, 2000; ISBN 978-0-12-257060-5.
4. Gilbert, M.; Masters, W.P.E. *Introduction to Environmental Engineering and Science*, 3rd ed.; Prentice-Hall: London, UK, 2008; pp. 327–452. ISBN 0131481932.
5. United States Environmental Protection Agency. Clean Air Act Text. Available online: <https://www.epa.gov/clean-air-act-overview/clean-air-act-text> (accessed on 10 March 2018).
6. Zhao, X.; Cai, Q.; Ma, C.; Hu, Y.; Luo, K.; Li, W. Economic evaluation of environmental externalities in China's coal-fired power generation. *Energy Policy* **2017**, *102*, 307–317. [CrossRef]
7. Berenjian, A.; Chan, N.; Malmiri, H.J. Volatile Organic Compounds Removal Methods: A Review. *Am. J. Biochem. Biotechnol.* **2012**, *8*, 220–229. [CrossRef]
8. Fu, X.; Liu, Y.; Yao, W.; Wu, Z. One-step synthesis of bimetallic Pt-Pd/MCM-41 mesoporous materials with superior catalytic performance for toluene oxidation. *Catal. Commun.* **2016**, *83*, 22–26. [CrossRef]
9. Tomatis, M.; Xu, H.H.; He, J.; Zhang, X.D. Recent Development of Catalysts for Removal of Volatile Organic Compounds in Flue Gas by Combustion: A Review. *J. Chem.* **2016**, 8324826. [CrossRef]
10. Ryoo, M.-W.; Chung, S.-G.; Kim, J.-H.; Song, Y.S.; Seo, G. The effect of mass transfer on the catalytic combustion of benzene and methane over palladium catalysts supported on porous materials. *Catal. Today* **2003**, *83*, 131–139. [CrossRef]
11. Wang, Y.; Dai, C.; Chen, B.; Wang, Y.; Shi, C.; Guo, X. Nanoscale HZSM-5 supported PtAg bimetallic catalysts for simultaneous removal of formaldehyde and benzene. *Catal. Today* **2015**, *258*, 616–626. [CrossRef]
12. Azalim, S.; Franco, M.; Brahmi, R.; Giraudon, J.M.; Lamonier, J.F. Removal of oxygenated volatile organic compounds by catalytic oxidation over Zr-Ce-Mn catalysts. *J. Hazard. Mater.* **2011**, *188*, 422–427. [CrossRef] [PubMed]
13. Jiang, S.J.; Song, S.Q. Enhancing the performance of $\text{Co}_3\text{O}_4/\text{CNTs}$ for the catalytic combustion of toluene by tuning the surface structures of CNTs. *Appl. Catal. B* **2013**, *140*, 1–8. [CrossRef]
14. Urbutis, A.; Kitrys, S. Dual function adsorbent-catalyst $\text{CuO-CeO}_2/\text{NaX}$ for temperature swing oxidation of benzene, toluene and xylene. *Cent. Eur. J. Chem.* **2014**, *12*, 492–501. [CrossRef]
15. Zhou, G.L.; Gui, B.G.; Xie, H.M.; Yang, F.; Chen, Y.; Chen, S.M.; Zheng, X.X. Influence of CeO_2 morphology on the catalytic oxidation of ethanol in air. *J. Ind. Eng. Chem.* **2014**, *20*, 160–165. [CrossRef]
16. Yang, P.; Shi, Z.; Yang, S.; Zhou, R. High catalytic performances of $\text{CeO}_2\text{-CrOx}$ catalysts for chlorinated VOCs elimination. *Chem. Eng. Sci.* **2015**, *126*, 361–369. [CrossRef]

17. Rotter, H.; Landau, M.V.; Herskowitz, M. Combustion of Chlorinated VOC on Nanostructured Chromia Aerogel as Catalyst and Catalyst Support. *Environ. Sci. Technol.* **2005**, *39*, 6845–6850. [[CrossRef](#)] [[PubMed](#)]
18. Bendahou, K.; Cherif, L.; Siffert, S.; Tidahy, H.L.; Benaissa, H.; Aboukais, A. The effect of the use of lanthanum-doped mesoporous SBA-15 on the performance of Pt/SBA-15 and Pd/SBA-15 catalysts for total oxidation of toluene. *Appl. Catal. A* **2008**, *351*, 82–87. [[CrossRef](#)]
19. Liu, Z.S.; Chen, J.Y.; Peng, Y.H. Activated carbon fibers impregnated with Pd and Pt catalysts for toluene removal. *J. Hazard. Mater.* **2013**, *256–257*, 49–55. [[CrossRef](#)] [[PubMed](#)]
20. Salameh, S.I.Y.; Khalili, F.I.; Al-Dujaili, A.H. Removal of U(VI) and Th(IV) from aqueous solutions by organically modified diatomaceous earth: Evaluation of equilibrium, kinetic and thermodynamic data. *Int. J. Miner. Process.* **2017**, *168*, 9–18. [[CrossRef](#)]
21. Yusan, S.; Bampaiti, A.; Aytas, S.; Erenturk, S.; Aslani, M.A.A. Synthesis and structural properties of ZnO and diatomite-supported ZnO nanostructures. *Ceram. Int.* **2016**, *42*, 2158–2163. [[CrossRef](#)]
22. Huang, X.L.; Catignani, G.L.; Swaisgood, H.E. Comparison of the properties of trypsin immobilized on 2 Celite™ derivatives. Paper No. FSR 95-4 of the Journal Series of the Department of Food Science, North Carolina State University, Raleigh, NC 27695-7624. The use of trade names in this publication does not imply endorsement by the North Carolina Agricultural Research Service of the products named, nor criticism of similar ones not mentioned. *J. Biotechnol.* **1997**, *53*, 21–27. [[CrossRef](#)] [[PubMed](#)]
23. Chang, S.-F.; Chang, S.-W.; Yen, Y.-H.; Shieh, C.-J. Optimum immobilization of *Candida rugosa* lipase on Celite by RSM. *Appl. Clay Sci.* **2007**, *37*, 67–73. [[CrossRef](#)]
24. Giton, F.; Guehot, J.; Fiet, J. New reusable Celite/ethylene glycol cartridges for selective chromatography of steroids before immunoassay. *Clin. Biochem.* **2009**, *42*, 1735–1738. [[CrossRef](#)] [[PubMed](#)]
25. Rhodes, E.R.; Huff, E.M.; Hamilton, D.W.; Jones, J.L. The evaluation of hollow-fiber ultrafiltration and celite concentration of enteroviruses, adenoviruses and bacteriophage from different water matrices. *J. Virol. Methods* **2016**, *228*, 31–38. [[CrossRef](#)] [[PubMed](#)]
26. Zhou, G.; He, X.; Liu, S.; Xie, H.; Fu, M. Phenyl VOCs catalytic combustion on supported CoMn/AC oxide catalyst. *J. Ind. Eng. Chem.* **2015**, *21*, 932–941. [[CrossRef](#)]
27. Zuo, S.; Wang, X.; Yang, P.; Qi, C. Preparation and high performance of rare earth modified Pt/MCM-41 for benzene catalytic combustion. *Catal. Commun.* **2017**, *94*, 52–55. [[CrossRef](#)]
28. Tamaddon, F.; Nasiri, A.; Farokhi, S. CsF–Celite as an efficient heterogeneous catalyst for sulfonylation and desulfonylation of heteroatoms. *Catal. Commun.* **2011**, *12*, 1477–1482. [[CrossRef](#)]
29. Kumar, A.; Kanwar, S.S. Synthesis of ethyl ferulate in organic medium using celite-immobilized lipase. *Bioresour. Technol.* **2011**, *102*, 2162–2167. [[CrossRef](#)] [[PubMed](#)]
30. Mudliar, S.; Giri, B.; Padoley, K.; Satpute, D.; Dixit, R.; Bhatt, P.; Pandey, R.; Juwarkar, A.; Vaidya, A. Bioreactors for treatment of VOCs and odours—A review. *J. Environ. Manag.* **2010**, *91*, 1039–1054. [[CrossRef](#)] [[PubMed](#)]
31. Yuan, P.; Wu, D.Q.; He, H.P.; Lin, Z.Y. The hydroxyl species and acid sites on diatomite surface: a combined IR and Raman study. *Appl. Surf. Sci.* **2004**, *227*, 30–39. [[CrossRef](#)]
32. Wang, Z.; Yang, Y.; Qu, X.; Zhang, J.; Chen, Y.; Nie, L. Decolouring mechanism of Zhejiang diatomite. Application to printing and dyeing wastewater. *Environ. Chem. Lett.* **2005**, *3*, 33–37. [[CrossRef](#)]
33. Dehestaniathar, S.; Khajelakzay, M.; Ramezani-Farani, M.; Ijadpanah-Saravi, H. Modified diatomite-supported CuO-TiO₂ composite: Preparation, characterization and catalytic CO oxidation. *J. Taiwan Inst. Chem. Eng.* **2016**, *58*, 252–258. [[CrossRef](#)]
34. Sun, Q.; Li, H.; Zheng, S.; Sun, Z. Characterizations of nano-TiO₂/diatomite composites and their photocatalytic reduction of aqueous Cr(VI). *Appl. Surf. Sci.* **2014**, *311*, 369–376. [[CrossRef](#)]
35. Beauchet, R.; Magnoux, P.; Mijoin, J. Catalytic oxidation of volatile organic compounds (VOCs) mixture (isopropanol/*o*-xylene) on zeolite catalysts. *Catal. Today* **2007**, *124*, 118–123. [[CrossRef](#)]
36. Pinard, L.; Tayeb, K.B.; Hamieh, S.; Vezin, H.; Canaff, C.; Maury, S.; Delpoux, O.; Pouilloux, Y. On the involvement of radical “coke” in ethanol conversion to hydrocarbons over HZSM-5 zeolite. *Catal. Today* **2013**, *218–219*, 57–64. [[CrossRef](#)]
37. Guisnet, M.; Magnoux, P. Coking and deactivation of zeolites. *Appl. Catal.* **1989**, *54*, 1–27. [[CrossRef](#)]
38. Wyrwalski, F.; Lamonier, J.F.; Siffert, S.; Aboukais, A. Additional effects of cobalt precursor and zirconia support modifications for the design of efficient VOC oxidation catalysts. *Appl. Catal. B* **2007**, *70*, 393–399. [[CrossRef](#)]

39. United States Environmental Protection Agency. Integrated Risk Information System (IRIS) on Benzene. In *Office of Research and Development*; National Center for Environmental, Ed.; United States Environmental Protection Agency: Washington, DC, USA, 2009.
40. Zhang, Z.; Shi, D. Purifying Process of Diatomaceous Earth through Flocculation and Magneto-Separation by Specific Gravity. Google Patent CN 1,045,252 A, 12 September 1990.
41. Wang, B. Diatomaceous Earth Products, Processes for Preparing them, and Methods of Their Use. Google Patent WO 2013096578 A1, 27 June 2013.
42. Sarangi, M.; Nayak, P.; Tiwari, T.N. Effect of temperature on nano-crystalline silica and carbon composites obtained from rice-husk ash. *Compos. Part B* **2011**, *42*, 1994–1998. [[CrossRef](#)]
43. Li, W.B.; Zhuang, M.; Wang, J.X. Catalytic combustion of toluene on Cu-Mn/MCM-41 catalysts: Influence of calcination temperature and operating conditions on the catalytic activity. *Catal. Today* **2008**, *137*, 340–344. [[CrossRef](#)]
44. Anderson, J.R. Particle-Size Effects in Metal-Catalysts. *Sci. Prog.* **1985**, *69*, 461–484.
45. Isaifan, R.J.; Ntais, S.; Baranova, E.A. Particle size effect on catalytic activity of carbon-supported Pt nanoparticles for complete ethylene oxidation. *Appl. Catal. A* **2013**, *464–465*, 87–94. [[CrossRef](#)]
46. Ustinov, E.A. Nitrogen adsorption on silica surfaces of nonporous and mesoporous materials. *Langmuir* **2008**, *24*, 6668–6675. [[CrossRef](#)] [[PubMed](#)]
47. Liu, C.; Gong, L.; Dai, R.; Lu, M.; Sun, T.; Liu, Q.; Huang, X.; Huang, Z. Mesoporous Mn promoted Co_3O_4 oxides as an efficient and stable catalyst for low temperature oxidation of CO. *Solid State Sci.* **2017**, *71*, 69–74. [[CrossRef](#)]
48. Zhang, X.; Li, H.; Hou, F.; Yang, Y.; Dong, H.; Liu, N.; Wang, Y.; Cui, L. Synthesis of highly efficient Mn_2O_3 catalysts for CO oxidation derived from Mn-MIL-100. *Appl. Surf. Sci.* **2017**, *411*, 27–33. [[CrossRef](#)]
49. Saqer, S.M.; Kondarides, D.I.; Verykios, X.E. Catalytic Activity of Supported Platinum and Metal Oxide Catalysts for Toluene Oxidation. *Top. Catal.* **2009**, *52*, 517–527. [[CrossRef](#)]
50. Basińska, A.; Józwiak, W.K.; Góralski, J.; Domka, F. The behaviour of Ru/ Fe_2O_3 catalysts and Fe_2O_3 supports in the TPR and TPO conditions. *Appl. Catal. A* **2000**, *190*, 107–115. [[CrossRef](#)]
51. Nogueira, F.G.E.; Lopes, J.H.; Silva, A.C.; Lago, R.M.; Fabris, J.D.; Oliveira, L.C.A. Catalysts based on clay and iron oxide for oxidation of toluene. *Appl. Clay Sci.* **2011**, *51*, 385–389. [[CrossRef](#)]
52. Li, D.; Li, C.; Suzuki, K. Catalytic oxidation of VOCs over Al- and Fe-pillared montmorillonite. *Appl. Clay Sci.* **2013**, *77–78*, 56–60. [[CrossRef](#)]
53. Liang, X.; Qi, F.; Liu, P.; Wei, G.; Su, X.; Ma, L.; He, H.; Lin, X.; Xi, Y.; Zhu, J.; et al. Performance of Ti-pillared montmorillonite supported Fe catalysts for toluene oxidation: The effect of Fe on catalytic activity. *Appl. Clay Sci.* **2016**, *132–133*, 96–104. [[CrossRef](#)]
54. Sexton, B.A.; Hughes, A.E.; Turney, T.W. An Xps and Tpr Study of the Reduction of Promoted Cobalt Kieselguhr Fischer-Tropsch Catalysts. *J. Catal.* **1986**, *97*, 390–406. [[CrossRef](#)]
55. Tang, C.-W.; Wang, C.-B.; Chien, S.-H. Characterization of cobalt oxides studied by FT-IR, Raman, TPR and TG-MS. *Thermochim. Acta* **2008**, *473*, 68–73. [[CrossRef](#)]
56. Stobbe, E.R.; de Boer, B.A.; Geus, J.W. The reduction and oxidation behaviour of manganese oxides. *Catal. Today* **1999**, *47*, 161–167. [[CrossRef](#)]
57. Brummer, V.; David, J.; Martinec, J.; Lestinsky, P.; Skryja, P.; Stehlík, P. Impact of catalytic oxidation operating conditions on VOC and Co conversions on the Pt-Pd/ Al_2O_3 catalyst. *Chem. Eng. Trans.* **2015**, *45*, 1009–1014. [[CrossRef](#)]
58. Pinard, L.; Hamieh, S.; Canaff, C.; Ferreira Madeira, F.; Batonneau-Gener, I.; Maury, S.; Delpoux, O.; Ben Tayeb, K.; Pouilloux, Y.; Vezin, H. Growth mechanism of coke on HBEA zeolite during ethanol transformation. *J. Catal.* **2013**, *299*, 284–297. [[CrossRef](#)]
59. Rojo-Gama, D.; Signorile, M.; Bonino, F.; Bordiga, S.; Olsbye, U.; Lillerud, K.P.; Beato, P.; Svelle, S. Structure–deactivation relationships in zeolites during the methanol-to-hydrocarbons reaction: Complementary assessments of the coke content. *J. Catal.* **2017**, *351*, 33–48. [[CrossRef](#)]
60. Schulz, H. “Coking” of zeolites during methanol conversion: Basic reactions of the MTO-, MTP- and MTG processes. *Catal. Today* **2010**, *154*, 183–194. [[CrossRef](#)]
61. Li, W.B.; Zhuang, M.; Xiao, T.C.; Green, M.L. MCM-41 supported Cu-Mn catalysts for catalytic oxidation of toluene at low temperatures. *J. Phys. Chem. B* **2006**, *110*, 21568–21571. [[CrossRef](#)] [[PubMed](#)]
62. Guisnet, M.; Magnoux, P. Organic chemistry of coke formation. *Appl. Catal. A* **2001**, *212*, 83–96. [[CrossRef](#)]

63. Zhao, H.; Luo, X.; He, J.; Peng, C.; Wu, T. Recovery of elemental sulphur via selective catalytic reduction of SO₂ over sulphided CoMo/ γ -Al₂O₃ catalysts. *Fuel* **2015**, *147*, 67–75. [[CrossRef](#)]
64. Zhang, K.; Liu, Y.Q.; Tian, S.; Zhao, E.H.; Zhang, J.C.; Liu, C.G. Preparation of bifunctional NiPb/ZnO-diatomite-ZSM-5 catalyst and its reactive adsorption desulfurization coupling aromatization performance in FCC gasoline upgrading process. *Fuel* **2013**, *104*, 201–207. [[CrossRef](#)]
65. Thommes, M.; Kaneko, K.; Neimark, A.V.; Olivier, J.P.; Rodriguez-Reinoso, F.; Rouquerol, J.; Sing, K.S.W. Physisorption of gases, with special reference to the evaluation of surface area and pore size distribution (IUPAC Technical Report). *Pure Appl. Chem.* **2015**, *87*. [[CrossRef](#)]
66. Saqer, S.M.; Kondarides, D.I.; Verykios, X.E. Catalytic oxidation of toluene over binary mixtures of copper, manganese and cerium oxides supported on γ -Al₂O₃. *Appl. Catal. B* **2011**, *103*, 275–286. [[CrossRef](#)]



© 2018 by the authors. Licensee MDPI, Basel, Switzerland. This article is an open access article distributed under the terms and conditions of the Creative Commons Attribution (CC BY) license (<http://creativecommons.org/licenses/by/4.0/>).